

Optimization of high voltage-type solar cell comprising thin TiO₂ on anode and thin Ag–TiO₂ photocatalysts on cathode

Kazuki Urushidate^{a,1}, Keisuke Hara^{a,1}, Mao Yoshiba^{a,1}, Takashi Kojima^b, Takaomi Itoi^c, Yasuo Izumi^{a,*}

^a Department of Chemistry, Graduate School of Science, Chiba University, Yayoi 1-33, Inage-ku, Chiba 263-8522, Japan

^b Department of Applied Chemistry and Biotechnology, Graduate School of Engineering, Chiba University Yayoi 1-33, Inage-ku, Chiba 263-8522, Japan

^c Department of Mechanical Engineering, Graduate School of Engineering, Chiba University, Yayoi 1-33, Inage-ku, Chiba 263-8522, Japan

ARTICLE INFO

Keywords:

Ag nanoparticle
Photocatalyst
Photocathode
High voltage
Solar cell
EXAFS

ABSTRACT

A high-voltage type solar cell consisting of a TiO₂ photocatalyst on the anode, an Ag–TiO₂ photocatalyst on the cathode, and the water/O₂ redox system is enabled and optimized by controlling the Ag size (~4 nm) and core-shell structure at the proximity of the indium tin oxide cathode, the photocatalyst film thickness (3.1 ± 0.3 μm), and the configuration of photoelectrodes in the solar cell (SC). The active sites for O₂ photoreduction were Ag⁰ in situ formed on cathode irradiated by UV–visible light as evidenced by Ag K-edge extended X-ray absorption fine structure. Ag–Ag coordination number increased from 1.6 under aqueous HCl electrolyte to 9.6–11 under the conditions of SC tests, suggesting homogeneous Ag size distribution and maximized Ag⁰ active sites. The effective Ag⁰ shell was present only under the irradiation of UV–visible light; Ag⁰ sites were transformed into Ag₂O sites when the light was turned off. By the optimization of Ag content and Ag–TiO₂ film thickness on photocathode and light irradiation configuration from photocatalyst/electrode side on anode/cathode, an open-circuit voltage of 1.55 V exceeding most of the SC reported so far. Furthermore, cell power of 18.7 μW cm⁻² was also achieved.

1. Introduction

Solar cells (SCs) and fuel cells (FCs) are key technology for a sustainable society. In their applications, the electromotive force is, in general, less than 1 V per cell, and stacking of the cells is inevitable to realize the voltage required for practical purposes. In particular, the photocathode has been intensively studied for water splitting to produce H₂ [Paracchino et al., 2011; Jia et al., 2012]. In this paper, SC utilizing thin TiO₂ photocatalyst on anode and thin Ag–TiO₂ photocatalyst on cathode is demonstrated to realize an electromotive force of 3.00 V per cell in principle (Scheme 1). The principle is to obtain a maximum electromotive force between the conduction band (CB) minimum of TiO₂ and the valence band (VB) maximum of [Ag–]TiO₂, in clear contrast to the electromotive force below 1 V between the oxidation and reduction reaction potential at anode and cathode that is obtained for silicon SCs, dye-sensitized SCs, and FCs [Fujishima et al., 2015].

The reactions occurring on anode and cathode are as follows. The reaction potential E^\ominus is 1.11 V at standard hydrogen electrode (SHE), pH

2 for these reactions.

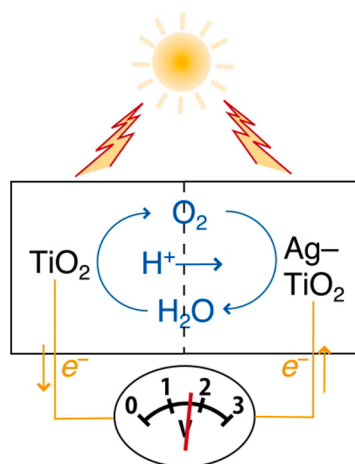


The reactions (1) and (2) proceed on TiO₂ and Ag–TiO₂ photocatalyst films, respectively (Scheme 1). In contrast that the theoretical electromotive force is limited to 2.75 V when thin TiO₂ and BiOCl films were used in the system controlled by the CB minimum of anatase-type TiO₂ (–0.11 V @SHE, @pH 2) and VB maximum of BiOCl (2.64 V @SHE, @pH 2) [Fujishima et al., 2015; Yoshiba et al., 2017; Urushidate et al., 2020], greater theoretical electromotive force is expected up to 3.00 V when thin TiO₂ and Ag–TiO₂ films are employed controlled by the CB minimum of anatase-type TiO₂ (–0.11 V) and VB maximum of [Ag–]TiO₂ (2.89 V). Furthermore, based on the crystal size and shape control of TiO₂, stable, flat, very thin Ag–TiO₂ film can be easily formed in contrast to fragile, flat, thin film of flake-like crystal of BiOCl [Fujishima et al., 2015; Yoshiba et al., 2017; Urushidate et al., 2020].

* Corresponding author.

E-mail address: yizumi@faculty.chiba-u.jp (Y. Izumi).

¹ These three authors contributed equally to this paper.



Scheme 1. Conceptual illustration of SC utilizing TiO_2 on anode and Ag-TiO_2 on cathode to enable 1.55 V per cell.

Furthermore, the size and core-shell structure of Ag nanoparticles were completely monitored by X-ray spectroscopy on the photocathode of a high voltage (HV)-type SC. The configuration of two photoelectrodes was optimized and the stability of the photocatalyst was demonstrated. The effects of the optimum (mean) distance between the Ag core-shell nanoparticles and the cathode electrode in the HV-type SC were evaluated by performing SC tests irradiating the photocatalyst side or the transparent electrode side, and active site analysis by extended X-ray absorption fine structure (EXAFS). The advantage to use EXAFS to monitor the Ag sites is to discriminate the composition of core and shell, and further to understand the active shell site structure under operation conditions of the SC.

2. Experimental section

2.1. Catalyst preparation

To prepare the Ag-TiO_2 photocatalyst, Ag nitrate was impregnated with TiO_2 [P25, Evonik, Essen, Germany; anatase/rutile phase = 8/2, specific surface area (SA) $60 \text{ m}^2 \text{ g}^{-1}$] from an aqueous suspension, dried at 373 K for 24 h, and heated in air at 673 K for 2 h [Misra et al., 2017]. The yellow color suggested the exclusive Ag^0 state. The Ag content was 1.0, 3.0, and 5.0 wt%. This sample is denoted as Ag-TiO_2 . After exposure to air overnight, the color changed to purple due to slow oxidation of metallic Ag^0 to Ag_2O .

Next, 0.4 mg of Ag-TiO_2 powder was well mixed with 1.0 mL of *t*-butanol, and ethylene glycol was added as a thickener. The suspension was ultrasonicated (430 W, 38 kHz) for 10 min. The paste (36 μL) was extended to a thin film (thickness, 3.1 μm ; area, $1.0 \times 1.3 \text{ cm}^2$) on an indium tin oxide (ITO; thickness, 0.12–0.16 μm ; sheet resistivity, 8–12 Ω/square)-coated Pyrex glass plate (Sigma-Aldrich, St. Louis, MO, USA) by slide method [Urushidate et al., 2020, 2018]. The $\text{Ag-TiO}_2/\text{ITO}/\text{Pyrex}$ plate was dried in air at 373 K for 18 h. The temperature was then increased to 573 K at a rate of 4 K min^{-1} and maintained at 573 K for 30 min. The photocatalyst area (1.3 cm^2) was adjusted to the size of UV-visible light spot on cathode photocatalyst in SC (see the Section 2.3). The mean thickness of Ag (3.0 wt%)- TiO_2 film was varied between 1.0 and 10 μm for optimization. The bulk density of Ag-TiO_2 (1.0 g cm^{-3}) was relatively low and advantageous for the use in SC in comparison to value for BiOCl photocatalyst ($5.6 \pm 1.8 \text{ g cm}^{-3}$) on cathode [Urushidate et al., 2018]. Thus-prepared $\text{Ag-TiO}_2/\text{ITO}/\text{Pyrex}$ plate was used as cathode while $\text{TiO}_2/\text{ITO}/\text{Pyrex}$ plate prepared in a similar procedure starting from TiO_2 (P25) was used as anode.

TiO_2 (JRC-TIO-6, purity >99%) was supplied by Sakai Chemical Industry Co. (Osaka, Japan). It was rutile crystals, and the specific SA

was $96.4 \text{ m}^2 \text{ g}^{-1}$. It was used to prepare Ag-TiO_2 film in comparison to using P25 TiO_2 .

2.2. Characterization

Transmission electron microscopy (TEM) observations were performed using a model JEM-2100F (JEOL, Tokyo, Japan) equipped with a field emission gun at an acceleration voltage of 200 kV. Ag-TiO_2 powder (10 mg) was dispersed in a *t*-butanol (5 mL) and ethylene glycol (0.06 mL) solution. The suspension was dropped and dried on a Cu mesh (150 meshes per inch) coated with a copolymer film of poly(vinyl alcohol) and formaldehyde (Formvar, Monsanto, St. Louis, MO, USA), and coated with carbon in a similar manner to the film formation via slide method on the ITO/Pyrex plate.

Cross-sectional scanning electron microscopy (SEM) images were obtained using a JSM-6510 scanning electron microscope (JEOL) at an accelerating voltage of 15 kV. A tungsten filament was used in the electron gun. The photocatalyst film on the ITO/Pyrex plate was cut and mounted on an aluminum sample holder using an adhesive. The incident angle of electrons with reference to the sample surface was between 5° and 15° . The magnification was between $\times 500$ and $\times 20,000$.

Ag K-edge EXAFS spectra were obtained at 290 K using a Si (311) double-crystal monochromator in the Photon Factory Advanced Ring at the High Energy Accelerator Research Organization (Tsukuba, Japan) on beamline NW10A [Zhang et al., 2019a]. The storage ring energy was 6.5 GeV and the ring current was 42.2 mA. A Si(311) double-crystal monochromator and Pt-coated focusing bent cylindrical mirror was inserted into the X-ray beam to obtain a beam of 1 mm (vertical) \times 2 mm (horizontal) size. X-ray intensity was maintained at 67% of the maximum flux using a piezo translator attached to the crystal to suppress higher harmonics. A photocatalyst film on ITO/Pyrex plate was placed in a sealable thin transparent Nylon bag and taken to a Lytle detector for fluorescence detection measurements [Lytle et al., 1984]. The conditions of atmosphere (air, N_2 , and/or aqueous HCl electrolyte of pH 2.0) and UV-visible light irradiation/darkness were varied for each measurement.

The EXAFS data was analyzed using XDAP software package [Vaarkamp et al., 2006]. The empirical parameters for curve fit analyses were obtained for Ag metal (interatomic distance R of 0.2889 nm and the coordination number N of 12) [Lamble and King, 1986], AgCl (0.2775 nm and N of 6) [Beccara et al., 2002], and Ag_2O (0.2044 nm and N of 2) [Liu and Bassett, 1973] (Table 1a).

2.3. SC tests

Using thin films of TiO_2 on the ITO anode and Ag-TiO_2 on the ITO cathode, the current (i)-voltage (V) characteristic was investigated in the SC (Scheme 1). Each photoelectrode was immersed in aqueous HCl (40 mL, initial pH 2.0), and the two compartments were separated by a proton-conducting polymer film (Nafion, Dupont, Wilmington, DE, USA; 50- μm thick). N_2 and O_2 , respectively, were bubbled at a distance of 30 mm from the photoelectrode at a flow rate of 100 mL min^{-1} . Both photocatalysts were irradiated with UV-visible light through the quartz windows of the SC from a 500-W Xe arc lamp (SX-UID502XAM, Ushio, Japan) using a two-way V-shaped branched quartz fiber light guide (5 ϕ -2B-1000L, San-ei Electric Co., Japan) [Fujishima et al., 2015; Yoshida et al., 2017; Urushidate et al., 2020, 2018]. Furthermore, light irradiation from photocatalyst side (front configuration) and that from ITO electrode side (rear configuration) were compared both for photoanode and photocathode in the SC.

3. Results

3.1. TEM observation

The high-angle annular dark field scanning TEM (HAADF-STEM)

Table 1

Best curve fit results of Ag K-edge EXAFS for an Ag (3.0 wt%)–TiO₂ film formed on ITO/Pyrex under several conditions.

Entry	Sample	Ag–O	Ag–Cl	Ag–Ag	Goodness of fit	Ref
		R (nm)				
a	573 K heated in air (pale brown)	0.206	–	0.284	14	
		1.3		1.6		
b	Under aq. HCl (yellow)	0.207	0.266	–	0.72	
		0.2	2.9	–3.6		
c	Under light, aq. HCl, and N ₂ for 30 min (pale yellow)	0.215	0.260	0.288	33	
		0.3	2.9	11		
d	Under light, aq. HCl, and N ₂ for 45 min (pale yellow)	–	0.259	0.291	136	
			1.9	9.6		
e	Under darkness and aq. HCl, and O ₂ (pale brown)	0.213	0.264	0.290	91	
		1.1	2.3	9.7		
f	Ag foil			0.2889		Lamble and King, 1986
				12		
	AgCl		0.2775			Beccara et al., 2002
	Ag ₂ O	0.2044		0.334		Liu and Bassett, 1973
		2		12		

image of Ag (3.0 wt%)–TiO₂ is shown in Fig. 1a. Brighter Ag nanoparticles (arrows) were homogeneously dispersed in/on the matrix of TiO₂. Ag L α and L β fluorescence lines were detected in the energy dispersive X-ray spectra in almost equivalent intensity ratio to that of the Ti K β line over all the film area shown in Fig. 1a within various beam spots of $\Phi = 100$ nm, suggesting homogeneous distribution of Ag nanoparticles in the TiO₂ matrix.

The high-resolution (HR)-TEM image was also recorded (Fig. 1b). The lattice fringes (0.246 and 0.171 nm intervals) observed in the nanoparticle regions of ~ 4 nm corresponded to Ag₂O (200) and (220) planes [Wei et al., 2011; Li et al., 2016]. The lattice fringes in the wider region in Fig. 1b, left (0.351 nm interval) corresponded to anatase-type TiO₂ (101) planes.

The particle size distribution was examined mainly based on HR-TEM images, but also employing HAADF-STEM images to clarify the distribution of Ag₂O over TiO₂ (Fig. 1c). The mean particles size was 3.3 ± 0.7 nm and the most probable size was between 2.75 and 3.00 nm.

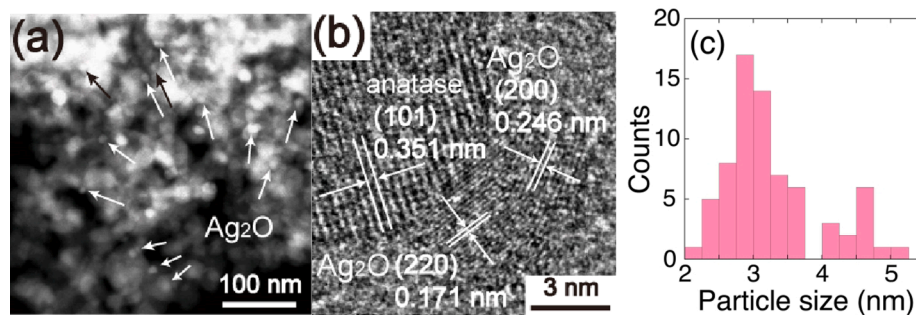


Fig. 1. (a) HAADF-STEM, (b) HR-TEM images, and the particle size distribution histogram of Ag₂O of the Ag (3.0 wt%)–TiO₂ film formed on a Cu mesh coated with Formvar and carbon.

3.2. Cross-sectional SEM observation

SEM images of Ag–TiO₂ films are shown in Fig. 2 formed on ITO/Pyrex plates via slide method. Based on the side view (Fig. 2a), the mean film thickness was 3.1 ± 0.3 μ m. Based on Eq. (3), the bulk density ρ of the Ag–TiO₂ film was calculated to be

$$\rho = \frac{(0.40 \pm 0.03) \times 10^{-3}}{(1.0 \times 1.3) \times (3.1 \pm 0.3) \times 10^{-4}} = 1.0 \pm 0.2 \text{ g cm}^{-3} \quad (3)$$

The Ag–TiO₂ film was relatively flat based on the top view (Fig. 2b).

3.3. EXAFS monitoring

For a fresh Ag (3.0 wt%)–TiO₂ thin film heated at 573 K in air, the Fourier-filtered angular photoelectron wavenumber k^3 -weighted EXAFS χ -function was fitted with two shells of Ag–O and Ag–Ag at 0.206 and 0.284 nm (Table 1a). The associated N value was 1.3 and 1.6, respectively, demonstrating major Ag₂O (N for bulk: 2) and minor metallic Ag⁰ phases (N for bulk: 12; Table 1f). This result is in accord with the color change of the fresh Ag–TiO₂ film from purple due to Ag₂O to pale brown after calcination (Fig. 3a), which corresponds to the mixture of Ag₂O (purple, major) and Ag⁰ (yellow, minor). The average particle size of Ag₂O and Ag⁰ was small for thin films ($3.1 \mu\text{m} \pm 0.3 \mu\text{m}$) because the N values of both Ag–O and Ag–Ag shells (1.3 and 1.6, respectively) were significantly smaller in comparison to values for bulk (2 and 12).

Next, the Ag–TiO₂ thin film on the ITO/Pyrex plate was immersed in aqueous HCl under N₂. The film color changed to yellow (Fig. 3b), and an Ag–Ag peak in air shifted slightly toward the Ag–Cl peak [Beccara

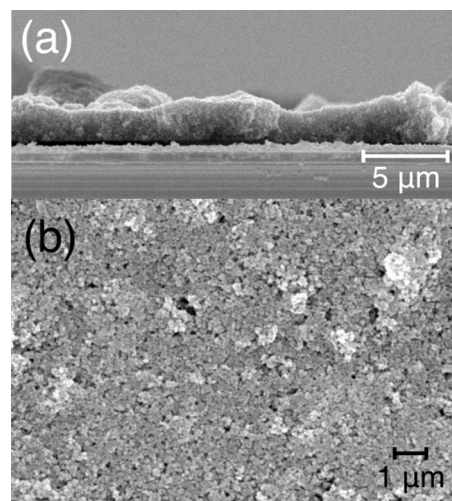


Fig. 2. Cross-sectional SEM images for Ag (3.0 wt%)–TiO₂. (A) Side view and (B) top view.

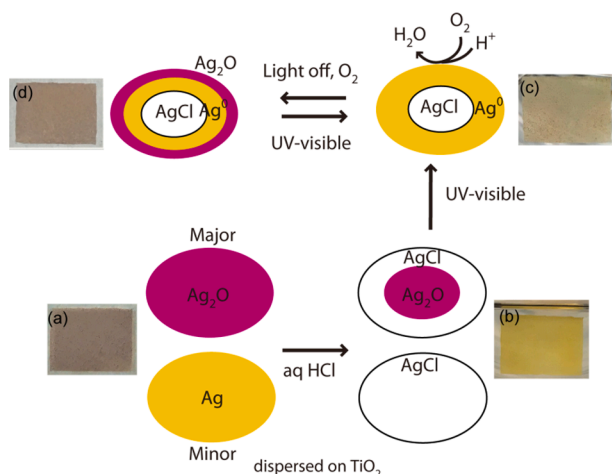


Fig. 3. Images displaying the changes of the Ag–TiO₂ thin film and model composition of Ag species (a–d) formed on an ITO/Pyrex glass plate under various conditions for SC test.

et al., 2002] in aqueous HCl. The N value for Ag–Cl was 2.9 (Table 1b). Although the Ag–O peak remained, the N value became as small as 0.2. In contrast, the Ag–Ag peak completely disappeared (Fig. S1). Accordingly, it can be concluded that most of the Ag₂O and Ag⁰ nanoparticles under air reacted predominantly with HCl to form AgCl (white or transparent). AgCl was inert for the photoreduction of O₂ on photocathode on SC, and the color change (Fig. 3) were nice indicator of reactivity because they were critically related photoreduction activity. A small amount of Ag₂O nanoparticles (purple) remained in the core of the AgCl shell, which explains the yellow color of the film (Fig. 3b).

In this study, the Ag–TiO₂ film thickness on ITO was as small as 3.1 ± 0.3 μm and Ag nanoparticles comprised of homogeneous size in the Ag–TiO₂ thin film: no Ag–Ag interatomic pair was found in the thin film under aqueous HCl (Table 1b).

Then, the Ag–TiO₂ thin film on the ITO/Pyrex plate was irradiated by UV–visible light from a 500-W xenon arc lamp at beamline. After 30 min, an Ag–Ag interatomic pair significantly evolved in the Fourier transform, and the N value became as great as 11 (Table 1c and Fig. S1), demonstrating the fast photoreduction of Ag⁺Cl to active Ag⁰ species for water photooxidation to O₂.

The photoreduction to metallic Ag⁰ was similar to reported Ag₂O photoreduction to Ag⁰ utilizing separated charge in TiO₂ by light [Albiter et al., 2015]. Because Ag⁰ is electrochemically favorable than Ag⁺ under the conditions of EXAFS measurements and SC tests (Section 3.5) [Van Cleve et al., 2016], experimental comparison of between Ag⁰ and Ag⁺ on O₂ reduction activity is difficult. However, as the catalytic role of Ag is to accept electrons from the CB of TiO₂ and to provide them to O₂ or the other oxidizing agent [Zhang et al., 2019a; Kawamura et al., 2017], electroconductive Ag⁰ shell is essential (Fig. 3c) and also advantageous by forming Schottky barrier to hold electrons from TiO₂ [Ogura et al., 2014]. In other words, the core of Ag component negligibly affected the photocatalysis on cathode.

The Ag–O shell in the Fourier transform (N of 0.3) that partially remained at 30 min completely disappeared at 45 min, whereas the minor Ag–Cl shell still remained (N of 1.9; Table 1d and Fig. S1) as the core for Ag⁰ shell (Fig. 3c).

The photocatalyst film color became pale yellow, reflecting the predominant metallic Ag⁰ shell. Although minor AgCl remained as the core (Fig. 3c), the N value changes for Ag–Ag pair by light were great (from 1.6 to 9.6–11, Table 1a, c, and d) related to enough thin film of 3.1 ± 0.3 μm well in contact with gas phase.

After the light was turned off, the sample bag was purged with O₂. The N value of Ag–Ag remained virtually unaltered; however, the Ag–O peak became evident due to the oxidation of Ag⁰ nanoparticles in O₂ (N

of 1.1, Table 1e). The film color became pale brown, as a passivation indicator due to the partial oxidation to Ag₂O (purple) over the AgCl@Ag⁰ core–shell structure (Fig. 3d), similar to the fresh film sample (Fig. 3a).

In summary, surface Ag sites changed the valence state adapting the environment: air, aqueous HCl, and sufficient electrons under light to exhibit the O₂ photoreduction activity. The resultant core–shell structure (Fig. 3c) is not optimization but adaption for the O₂ photoreduction. Conversely, active Ag⁰ shell was formed on cathode under UV–visible light, suggesting that the preparation conditions of Ag–TiO₂ composite negligibly affect the SC performance because any Ag and/or Ag₂O nanoparticles formed are transformed into AgCl and then to active Ag⁰ shell for the O₂ photoreduction (Fig. 3).

3.4. UV–visible spectra

Diffuse reflectance UV–visible spectra were measured for Ag (3.0 wt %)–TiO₂/ITO/Pyrex under various conditions during the SC test (Fig. 4). The data were the convolution of phase components of Ag core–shell nanoparticles (Fig. 3) and TiO₂. A broad peak ranging from 340 to 650 nm appeared for the fresh film, corresponding to the complementary color (green and blue) of sample color (pale brown; Fig. 3a and a). Next, a narrower peak from 350 to 570 nm appeared for the thin film treated with aqueous HCl and dried in N₂ due to the loss of Ag⁰ component (Fig. 4b), corresponding to the complementary color (purple) of sample color under the conditions (yellow; Fig. 3b).

Then, a red-shifted major peak ranging from 400 to 580 nm attributable to Ag⁰ (Fig. 4c) appeared for the thin film irradiated by UV–visible light, corresponding to the complementary color (pale purple) of sample under the conditions (pale yellow; Fig. 3c). The peak became weaker (Fig. 4c) because the data was taken after UV–visible light irradiation, and a part of Ag⁰ would re-oxidize in the UV–visible spectrometer.

Finally, a broader peak appeared in the range from 340 to 620 nm due to the presence of both Ag⁰ and Ag₂O (Fig. 4d) for the thin film subjected to darkness and dried in O₂ gas after irradiation, corresponding to the complementary color (green and blue) of sample color: pale brown under the conditions (Fig. 3d).

3.5. SC tests

First, UV–visible light was irradiated from the photocatalyst side both at anode and cathode, i.e., in a front–front configuration [Yoshida et al., 2017]. The open circuit voltage (V_{oc}) value was 1.45 V (Table 2a). When the cell voltage decreased to 0.3 V, the i value gradually increased to 5 μA cm⁻² (Fig. 5a, □). When the voltage became less than 0.2 V, the

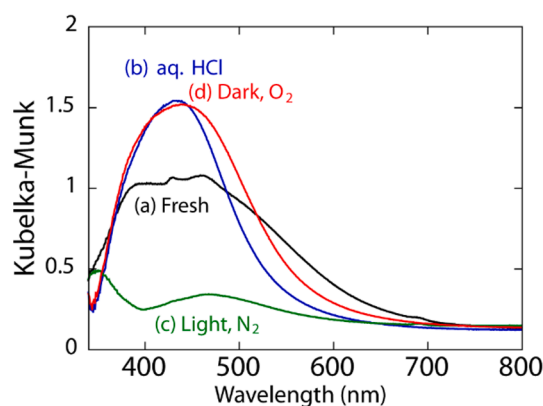


Fig. 4. Diffuse reflectance UV–visible spectra measured for Ag (3.0 wt%)–TiO₂/ITO/Pyrex under the following conditions: fresh (a), under aqueous HCl pH 2.0 and dried in N₂ gas (b), under UV–visible light and dried in N₂ gas (c), and under darkness and dried in O₂ gas (d).

current sharply increased from 7 to 27.8 $\mu\text{A cm}^{-2}$ (short-circuit current, i_{SC}) as a leakage current due to the electron flow from anode to cathode [Yoshida et al., 2017], then directly to Ag nanoparticles, and finally to reduce O_2 in combination with protons on surface Ag site (Fig. 3c). The maximum cell power (W_{max}) value was 2.8 $\mu\text{W cm}^{-2}$ (@0.92 V, 3.1 $\mu\text{A cm}^{-2}$; Table 2a).

Next, the front (anode)–rear (cathode) configuration was tested (Fig. 5a, ○). The performance was significantly improved, drawing an ideal convex curve for the SC in the wider voltage range of 0.35–1.55 V. However, the current increased linearly up to 34.9 $\mu\text{A cm}^{-2}$ below 0.3 V (Fig. 5a, ○ and Table 2b) due to the leakage current. The voltage (0.27 V) was the difference between the CB of TiO_2 (−0.11 V) and the Fermi level of Ag (+0.16 V versus SHE). Thus, the V_{oc} value of 1.55 V and W_{max} value of 18.7 $\mu\text{W cm}^{-2}$ were demonstrated using TiO_2 on anode and Ag– TiO_2 on cathode in the front and rear configuration, respectively.

In contrast, the cell performance values were minimal in the rear (anode)–front (cathode) configuration (Fig. 5b, □ and Table 2c). The performance in the rear–rear configuration was slightly less than that in the front–rear configuration. The order of W_{max} values was

front – rear > rear – rear >> front – front > rear – front,

demonstrating that rear configuration at cathode was essential. Secondly, front configuration at anode was favorable. Due to unknown reason, the V_{oc} value in rear–rear configuration was unexpectedly low (1.27 V; Fig. 5b, ○ and Table 2d). The lower photo-oxidative performance of rear configuration at anode may lower the V_{oc} value.

For the further optimization of SC, the Ag loading in photocatalyst was varied between 1.0 and 5.0 wt% (Table 2b, g, and h). The V_{oc} and W_{max} values were maximal at Ag 3.0 wt% (1.55 V and 18.7 $\mu\text{W cm}^{-2}$). Conversely, the i_{SC} values progressively increased nearly proportional to the amount of Ag in photocatalysts. Apparently, the electromotive force in this SC originates from the energy difference of CB of TiO_2 on anode and VB of [Ag–] TiO_2 on cathode (Scheme 1). The electromotive force originates from the charge separation in TiO_2 on both electrodes, but the excited electrons on anode transfer to cathode while the ones on cathode were injected to Ag then to O_2 [Ogura et al., 2014, 2015].

In this context, the electron trapping efficiency and the number of active site for O_2 photoreduction are improved as the Ag amount increases. For a SC test using Ag (5.0 wt%)– TiO_2 photocatalyst on cathode, cell current density sharply increased at less than 0.5 V (Fig. 5c) in comparison to moderate increase using photocatalysts of Ag 1.0 and 3.0 wt%. This is due to short-cut electron flow (current) starting from anode to ITO film of cathode, then directly Ag nanoparticles [Yoshida et al., 2017]. Based on two control factors, The V_{oc} and W_{max} values were maximal at Ag 3.0 wt%.

Furthermore, Ag (3.0 wt%)– TiO_2 photocatalyst film mean thickness on ITO cathode was varied between 1.0 and 10 μm (Table 2b, e, and f). The performance (V_{oc} and W_{max}) was nearly optimal when the mean thickness was 3.1–10 μm while the W_{max} value was significantly lower when the thickness was 1.0 μm (Fig. 5d). Instead, short-cut current

became significant at the voltage lower than 0.4 V, strongly suggesting direct electron insertion from ITO cathode into Ag nanoparticles for the thinner Ag– TiO_2 film. In comparison, negligible dependence of TiO_2 photocatalyst film thickness on anode was reported between 0.8 and 14.1 μm [Yoshida et al., 2017].

We also tried to optimize this SC by using different type of TiO_2 (rutile crystals, specific SA 96.4 $\text{m}^2 \text{g}^{-1}$) in comparison to P25 (anatase/rutile = 8/2, specific SA 60 $\text{m}^2 \text{g}^{-1}$) to prepare the photocatalyst used on cathode. The V_{oc} and W_{max} values 89–98% of values using P25 (Table 2b, i). The polarizability of crystal in photocatalyst film on cathode should be critical similar to TiO_2 film used on anode [Urushidate et al., 2018], but simple correlation between crystal phase, specific SA, and SC performance) was not found.

Furthermore, The other advantage of the Ag (3.0 wt%)– TiO_2 photocatalyst used on the cathode was demonstrated in repeated i – V tests at the interelectrode resistance between 500 k Ω and 0.3 Ω (Fig. 6). Using the combination of TiO_2 and Ag– TiO_2 on anode and cathode of the HV-SC, the W_{max} value gradually increased after three cycles and then converged to 18.7 $\mu\text{W cm}^{-2}$ after five cycles (Table 2b), whereas the combination of TiO_2 and BiOCl [Fujishima et al., 2015; Yoshida et al., 2017; Urushidate et al., 2020] decreased the W_{max} value by 7% after three cycles (Fig. 6b). The gradual increase of W_{max} value using Ag– TiO_2 on cathode (Fig. 6a) suggested optimum thickness of in situ formed Ag^0 shell for O_2 photoreduction (Fig. 3c). Under the test conditions, Ag– TiO_2 became stable after several cycles in contrast to gradual decreasing trend for BiOCl from the very early cycles.

The difference of W_{max} values using BiOCl rather than Ag– TiO_2 on cathode was 4.6 times under each best condition (Table 3). The difference is apparent, however, the increasing trend of power in 110 h is hopeful for better stability of Ag– TiO_2 for practical use rather than BiOCl .

4. Discussion

4.1. Advantage of thin Ag– TiO_2 film on cathode of SC

Thin TiO_2 and Ag– TiO_2 films ($3.1 \pm 0.3 \mu\text{m}$) were employed on ITO anode and cathode, respectively, in SC using photocatalysts. The electromotive force due to the energy difference between CB minimum of TiO_2 and VB maximum of [Ag–] TiO_2 (Scheme 1) was experimentally confirmed, associated with minimum overvoltage. The reasons of the overvoltage should be similar to SC using BiOCl on ITO cathode: charge (electrons, holes) diffusion in photocatalyst layer and at the interface between photocatalyst and ITO and the energy difference between CB minimum of TiO_2 (−0.11 V) and Fermi level of ITO (0.31 V@SHE) [Yoshida et al., 2017; Sugiyama et al., 2000].

The primary motivation of this study was to form thin homogeneous thickness film of TiO_2 and homogeneous sized Ag nanoparticles to maximize the catalysis on photoelectrodes (Scheme 1). TiO_2 thickness of 3.1–10 μm (Fig. 5d) and mean 4 nm of Ag nanoparticles (Figs. 1 and 5c)

Table 2
Best results of current (i)–voltage (V) tests for the high voltage-type SC.

Entry	Photocatalyst on anode	Photocatalyst on cathode			Configuration of photocatalysts (anode–cathode)	V_{oc} (V)	i_{sc} ($\mu\text{A cm}^{-2}$)	W_{max} ($\mu\text{W cm}^{-2}$)
		Type	Ag wt %	Mean thickness (μm)				
a	TiO_2 (P25, mean thickness 3.1 μm)	Ag– TiO_2 (P25)	3.0	3.1	Front–Front	1.45	27.8	2.8
b					Front–Rear	1.55	34.9	18.7
c					Rear–Front	0.53	22.5	1.3
d					Rear–Rear	1.27	39.2	12.4
e				1.0	Front–Rear	1.54	60.7	10.6
f						1.53	48.9	17.5
g						1.23	12.1	4.8
h						1.42	49.5	10.0
i		Ag– TiO_2 (JRC-6)	3.0			1.52	28.6	16.7

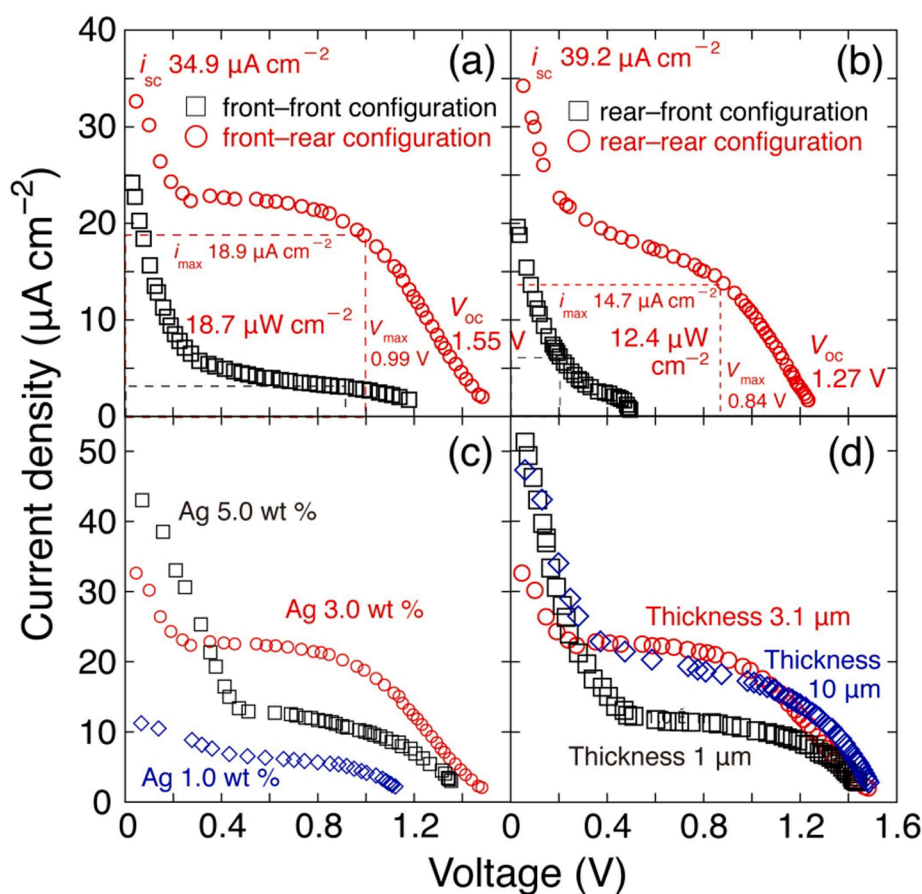


Fig. 5. Current (i)-voltage (V) dependence for a high voltage-type SC immersed in a HCl solution at pH 2.0, which comprises TiO₂ (mean thickness 3.1 μm) on the anode in front configuration (a) and rear configuration (b) and Ag (3.0 wt%)-TiO₂ (mean thickness 3.1 μm) on the cathode in front configuration (a, b, □) or rear configuration (a, b, ○); TiO₂ (mean thickness 3.1 μm) on the anode in front configuration and Ag-TiO₂ (Ag 1.0, 3.0, and 5.0 wt %; mean thickness 3.1 μm) on the cathode in rear configuration (c); and TiO₂ (mean thickness 3.1 μm) on the anode in front configuration and Ag-TiO₂ (Ag 3.0 wt%; mean thickness 1.0, 3.1, and 10 μm) on the cathode in rear configuration (d).

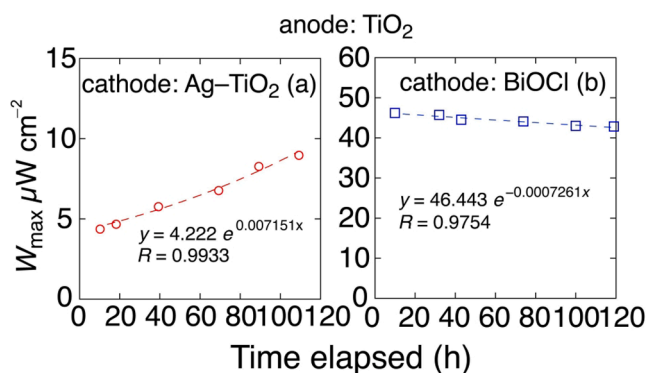


Fig. 6. Time course change of the W_{\max} value of the solar cell using TiO₂ (P25) on the anode (common) and Ag (3.0 wt%)-TiO₂ (a) or BiOCl (b) on the cathode. The interelectrode resistance changed from 500 kΩ to 0.3 Ω and back, constituting a cycle. Three cycles were repeated for the stability check of the photocatalysts.

were optimal for the SC. The key was to maintain stable Ag nanoparticles in TiO₂ matrix even the phase was consecutively converted in air (oxidized), in aq. HCl (chloridated), and under light (reduced to Ag⁰) (Fig. 3). Fragile hollow Ag nanosphere should be inappropriate.

We also formed photocatalyst film of Ag⁰-TiO₂ just heated in air at 673 K under argon (without contact to air) and/or Ag-TiO₂/ITO/Pyrex film just heated in air at 573 K was used in aqueous HCl in SC. In fact, the best SC performance in Fig. 5a (front-rear configuration) negligibly changed. Thus, core-shell structure was not the aim and the active Ag⁰ shell was always formed irradiated by light in contact with TiO₂ on cathode (Fig. 3c), but the ultimately small mean 4 nm of Ag

nanoparticles were the objective that was enabled in the enough thin homogeneous 3.1 μm thick of TiO₂ matrix.

The best V_{oc} value of 1.55 V and a cell power of 18.7 μW cm⁻² were achieved (Table 2b), superior to those obtained for similar SCs including TiO₂ and polyterthiophene (0.62, 0.90 V) [Zhang et al., 2017, 2019b], W-doped BiVO₄/Bi₄V₂O₁₁ and undoped BiVO₄/Bi₄V₂O₁₁ (1.54 V) [dos Santos et al., 2018] (Table 3).

Furthermore, stable increasing W_{\max} values as a function of time were observed using thin Ag-TiO₂ film on cathode (Fig. 6a), demonstrating the stability of Ag-TiO₂ photocatalyst in comparison to that of BiOCl (Fig. 6b). The stability of the active sites for the O₂ photoreduction reaction (Fig. 3c) is related to the different time course trend. The Ag⁰ sites were quickly in-situ formed on the shell under the SC test conditions (Table 1c and Fig. 3c). In contrast, proposed active site for the photoreduction reaction on BiOCl photocatalyst film, i.e. oxygen vacancy site, would be unstable depending on SC test conditions.

Conversely, the maximum V_{oc} value using TiO₂ and Ag-TiO₂ set (1.55 V) was unexpectedly lower than that using TiO₂ and BiOCl (1.96 V) [Urushidate et al., 2020] (Table 3) in contradiction to these theoretical values: 3.00 V and 2.75 V, respectively. One of the reasons is that Schottky barrier of <0.8 V [Walter et al., 2010; Zhang et al., 2012; Cowley et al., 1965] when the electrons should move from n-type TiO₂ matrix to Ag nanoparticle (further then to O₂ molecules combined with protons) should add extra overvoltage using TiO₂ and Ag-TiO₂ employed in this study. The diffusion overvoltage was estimated to be 0.23 V for thicker TiO₂ films [Yoshida et al., 2017], accounting for an overvoltage of 1.4 V in total.

In the comparison to the other SCs (Table 3), high voltage (1.55 V) per cell and no need to add fuel are the significant scientific advancement of this study. However, cell performance was lower compared to our SC using TiO₂ and BiOCl photocatalysts (Table 3). In this study, rear

Table 3
The comparison of solar cells and/or fuel cells using photocatalysts on both electrodes.

Photoanode	Photocathode	Fuel	V_{oc} (V)	W_{max} ($\mu\text{W cm}^{-2}$)	Ref.
TiO ₂	BiOCl	Acidic water	1.69	16.2	Fujishima et al., 2015
			1.91	42.2	Yoshida et al., 2017
			1.96	56.1	Urushidate et al., 2018
			1.94	85.2	Urushidate et al., 2020
			1.55	18.7	This work
CdS	Cu ₂ O	Phenol	0.62	60	Wu et al., 2015
			0.41	73	Wu et al., 2015
W:BiVO ₄	Polyterthiophene	Glucose	0.62	82	Zhang, 2017
			0.90	222	Zhang et al., 2019b
W-BiVO ₄ /Bi ₄ V ₂ O ₁₁	BiVO ₄ /Bi ₄ V ₂ O ₁₁	Na ₂ SO ₄ aq	1.54		dos Santos et al., 2018
BiVO ₄ /TiO ₂	Cu ₂ O/TiO ₂	Tetracycline hydrochloride	0.17		Lu et al., 2019
Ni-Fe LDH/BiVO ₄	Cu ₂ O/Cu	Methylene blue	0.65	74	He et al., 2019

configuration of photoanode significantly reduced V_{oc} value of SC and overvoltage due to the electron injection from TiO₂ CB into Ag was also suggested. These factors are not directly related to the principle of SC illustrated in Scheme 1 that proceeds via eqs (1) and (2). Thus, if the photocatalysts (TiO₂ on anode and the nanocomposite of TiO₂ and metal nanoparticles on cathode) are improved to maximize the rates of Eqs. (1) and (2) and for greater polarizability of photocatalyst films (Urushidate et al., 2020), even better SC performance is expected using TiO₂ and metal nanoparticles–TiO₂ compared to that using TiO₂ and BiOCl.

4.2. Optimization of the configurations of two photoelectrode

On the cathode of SC, electrons are excited at the band gap of TiO₂ irradiated by UV–visible light and trapped at Ag nanoparticles (Ogura et al., 2014). Metallic Ag⁰ sites are effective for the O₂ photoreduction, and in situ formation of Ag⁰ sites from Ag^ICl and Ag₂O under UV–visible light was demonstrated by EXAFS (Fig. 3 and Table 1c).

The difference of photoelectrode configuration as demonstrated in SC tests (Fig. 5) can be explained based on the diffusion length of electrons and holes (Scheme 2). In the front–front configuration (Fig. 5a, □), the oxygen reduction reaction occurred basically at the entire region in the thin Ag–TiO₂ photocatalyst films by charge-separated electrons created by UV–visible light irradiation, and the associated holes due to UV–visible light irradiation also populated the entire film region from the surface of the film to the interface between Ag–TiO₂ and ITO (Scheme 2a). Therefore, the electrons transferred from the anode must travel half the film thickness ($1/2 \times 3.1 \mu\text{m} = 1.5 \mu\text{m}$) in average to combine with holes at the cathode, or travel even longer if the O₂ reduction site populates relatively near the film surface (Scheme 2a) for the generation of the electromotive force.

In clear contrast, in the front–rear configuration (Fig. 5a, ○), the remaining holes due to O₂ photoreduction over Ag nanoparticles in proximity to the ITO electrode surface should combine very quickly with the electrons transported from the anode as illustrated in Scheme 2b.

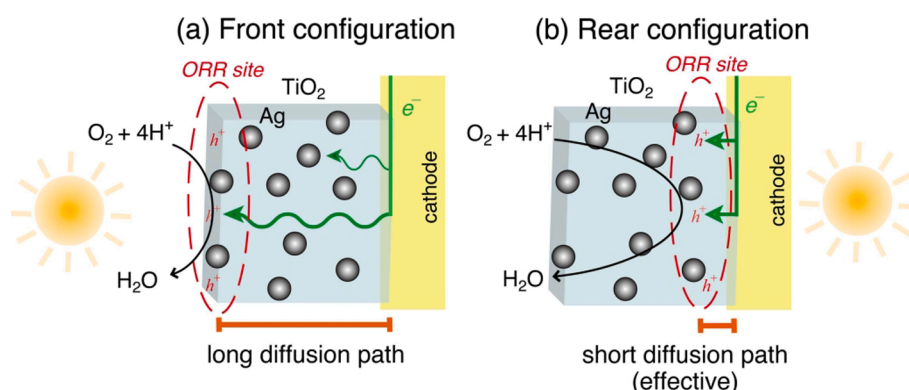
According to the comparison of the photoelectrode configurations to incident light, the O₂ photoreduction step proceeded faster than the electron diffusion in the Ag–TiO₂ film and/or at the interface between ITO and the Ag–TiO₂ films (Scheme 2). Therefore, the difference of the V_{oc} values (1.55 V in the front–rear configuration versus 1.45 V in the front–front configuration = 0.10 V; Table 2a, b) is exclusively due to electron diffusion overvoltage.

5. Conclusions

We prepared a $3.1 \pm 0.3\text{-}\mu\text{m}$ -thick Ag–TiO₂ film on the photocathode of a SC while TiO₂ film of similar thickness was used on the photoanode. The combination of TiO₂ on anode and Ag–TiO₂ on cathode, thinner films, optimized loading amount of Ag, and the homogeneous size distribution of the Ag nanoparticles allowed to transform most of the AgCl nanoparticle into AgCl@Ag⁰ core–shell structure maintaining the active Ag⁰ sites at the shell during the SC operation under UV–visible light based on the monitoring of Ag K-edge EXAFS, HR-TEM, and HAADF-STEM, resulting in a V_{oc} of 1.55 V and a W_{max} of $18.7 \mu\text{W cm}^{-2}$ per cell. The yellow color owing to the active Ag⁰ sites was a critical indicator of the photoreactivity in comparison to pale brown and white color due to the inert Ag₂O and AgCl sites, respectively. The gradual increase of W_{max} of SC containing Ag–TiO₂ on the cathode to converge to $18.7 \mu\text{W cm}^{-2}$ was demonstrated by repeated i – V tests in several hours, in contrast to 7% decrease of W_{max} for a cell containing BiOCl on the cathode in 2 h. The configuration of front–rear for the photoanode and photocathode, respectively, was also the key factor of cell power optimization due to the efficient charge coupling of SC at the interface between Ag–TiO₂ film and ITO film on the cathode.

Declaration of Competing Interest

The authors declare that they have no known competing financial interests or personal relationships that could have appeared to influence



Scheme 2. Proposed reaction in the Ag–TiO₂ film of the cathode in SC in the front–front (a) and front–rear configurations (b).

the work reported in this paper.

Acknowledgments

The authors are grateful for the financial support from the Grant-in-Aid for Scientific Research (17K05961, 20H02834) from Japan Society for Promotion of Science and Leading Research Promotion Program (2015–2019) from the Institute for Global Prominent Research, Chiba University. EXAFS experiments were performed with the approval of Photon Factory Proposal Review Committee (2018G649).

Appendix A. Supplementary material

Supplementary data to this article can be found online at <https://doi.org/10.1016/j.solener.2020.08.033>.

References

- Albiter, E., Valenzuela, M.A., Alfaro, S., Valverde-Aguilar, G., Martínez-Pallares, F.M., 2015. *J. Saudi Chem. Soc.* 19 (5), 563–573.
- Beccara, S.A., Dalba, G., Fornasini, P., Grisenti, R., Sanson, A., 2002. *Phys. Rev. Lett.* 89, 025503.
- Cowley, A.W., 1965. *J. Appl. Phys.* 36 (1065), 3212–3220.
- dos Santos, W.S., Rodriguez, M., Hhoury, J.M.O., Nascimento, J.A., Ribeiro, R.J.P., Mesquita, J.P., Silva, A.C., Nogueira, F.G.E., Pereira, M.C., 2018. *ChemSusChem* 11 (3), 589–597.
- Fujishima, Y., Ogura, Y., Tamba, M., Kojima, T., Izumi, Y., 2015. *J. Mater. Chem. A* 3, 8389–8404.
- He, Y., Zhang, C., Hu, J., Leung, M.K.H., 2019. *Energy Procedia* 158, 2188–2195.
- Jia, Q.X., Iwashina, K., Kudo, A., 2012. *Proc. Nat. Acad. Sci. U.S.A.* 109 (29), 11564–11569.
- Kawamura, S., Zhang, H., Tamba, M., Kojima, T., Miyano, M., Yoshida, Y., Yoshida, M., Izumi, Y., 2017. *J. Catal.* 345, 39–52.
- Lamble, G., King, D.A., 1986. *Phil. Trans. R. Soc. Lond.* 318, 203–217.
- Li, M.Y., Mao, Y.Q., Yang, S.K., Dai, T.T., Yang, H., Feng, F., Wu, T., Chen, M., Xu, G.Q., Wu, J.H., 2016. *ACS Omega* 1, 696–705.
- Liu, L.G., Bassett, W.A., 1973. *J. Appl. Phys.* 44, 1475–1479.
- Lu, Y., Chu, Y., Zheng, W., Huo, M., Huo, H., Qu, J., Yu, H., Zhao, Y., 2019. *Electrochim. Acta* 320, 134617.
- Lytle, F.W., Greeger, R.B., Sandstrom, D.R., Marques, E.C., Wong, J., Spiro, C.L., Huffman, G.P., Huggins, F.E., 1984. *Nucl. Instr. Meth. Phys. Resear.* 226, 542–548.
- Misra, M., Singh, N., Gupta, R.K., 2017. *Catal. Sci. Technol.* 7, 537–544.
- Ogura, Y., Yoshida, M., Izumi, Y., 2015. *Oil Gas Sci. Technol.* 70 (5), 853–862.
- Ogura, Y., Okamoto, S., Itoi, T., Fujishima, Y., Yoshida, Y., Izumi, Y., 2014. *Chem. Commun.* 50 (23), 3067–3070.
- Paracchino, A., Laporte, V., Sivula, K., Grätzel, M., Thimsen, E., 2011. *Nature Mater.* 10 (6), 456–461.
- Sugiyama, K., Ishii, H., Ouchi, Y., 2000. *Appl. Phys.* 87, 295.
- Urushidate, K., Li, J., Hara, K., Kojima, T., Izumi, Y., 2020. *ACS Sustain. Chem. Eng.* 8 (3), 1406–1416.
- Urushidate, K., Matsuzawa, S., Nakatani, K., Li, J., Kojima, T., Izumi, Y., 2018. *ACS Sustain. Chem. Eng.* 6, 11892–11903.
- M. Vaarkamp, H. Linders, D. Koningsberger, XDP Version 2.2.7; XAFS Services International, Woudenberg, The Netherlands, 2006.
- Van Cleve, T., Gibara, E., Linic, S., 2016. *ChemCatChem* 8 (1), 256–261.
- Walter, M.G., Warren, E.L., McKone, J.R., Boettcher, S.W., Mi, Q., Santori, E.A., Lewis, N.S., 2010. *Chem. Rev.* 110, 6446–6473.
- Wei, W., Mao, X., Ortiz, L.A., Sadoway, D.R., 2011. *J. Mater. Chem.* 21, 432–438.
- Wu, Z., Zhao, G., Zhang, Y., Liu, J., Zhang, Y.-N., Shi, H., 2015. *J. Mater. Chem. A* 3, 3416–3424.
- Yoshida, M., Ogura, Y., Tamba, M., Kojima, T., Izumi, Y., 2017. *RSC Advan.* 7 (32), 19996–20006.
- Zhang, H., Itoi, T., Konishi, T., Izumi, Y., 2019a. *J. Am. Chem. Soc.* 141, 6292–6301.
- Zhang, B., He, L., Yao, T., Fan, W., Zhang, X., Wen, S., Shi, J., Li, C., 2019b. *ChemSusChem* 12 (5), 1026–1032.
- Zhang, B., Fan, W., Yao, T., Liao, S., Li, A., Li, D., Liu, M., Shi, J., Liao, S., Li, C., 2017. *ChemSusChem* 10 (1), 99–105.
- Zhang, H., Ruan, S., Li, H., Zhang, M., Lv, K., Feng, C., Chen, W., 2012. *IEEE Electron Device Lett.* 33 (1), 83–85.